



Supporting Online Material for

Transient Simulation of Last Deglaciation with a New Mechanism for Bølling-Allerød Warming

Z. Liu,^{*} B. L. Otto-Bliesner, F. He, E. C. Brady, R. Tomas, P. U. Clark, A. E. Carlson, J. Lynch-Stieglitz, W. Curry, E. Brook, D. Erickson, R. Jacob, J. Kutzbach, J. Cheng

^{*}To whom correspondence should be addressed. E-mail: zliu3@wisc.edu

Published 17 July 2009, *Science* **325**, 310 (2009)
DOI: 10.1126/science.1171041

This PDF file includes:

Materials and Methods
SOM Text
Figs. S1 to S7
References and Notes

Other Supporting Online Material for this manuscript includes the following:
(available at www.sciencemag.org/cgi/content/full/325/5938/310/DC1)

Movie S1

Materials and Method

1: Model Setup: The CGCM employed is the National Center for Atmospheric Research (NCAR) CCSM3 with a dynamic global vegetation module. CCSM3 is a global, coupled ocean–atmosphere–sea ice–land surface climate model without flux adjustment (*S1*). All the simulations were performed in the version of T31_gx3v5 resolution (*S2*). The atmospheric model is the Community Atmospheric Model 3 (CAM3) with 26 hybrid coordinate levels in the vertical and ~3.75-degree resolution in the horizontal. The land model uses the same resolution as the atmosphere, and each grid box includes a hierarchy of land units, soil columns, and plant types. Glaciers, lakes, wetlands, urban areas, and vegetated regions can be specified in the land units. The ocean model is the NCAR implementation of the Parallel Ocean Program (POP) in vertical *z*-coordinate with 25 levels. The longitudinal resolution is 3.6-degree and the latitudinal resolution is variable, with finer resolution near the equator (~0.9 degrees). The sea ice model is the NCAR Community Sea Ice Model (CSIM). CSIM is a dynamic-thermodynamic model that includes a subgrid-scale ice thickness distribution. The resolution of CSIM is identical to that of POP. The preindustrial control simulation reproduces the major features of global climate, notably in the deep ocean (*S3*).

The Last Glacial Maximum (LGM) CCSM3 simulation has a global cooling of 4.5°C compared to pre-industrial with amplification of this cooling at high latitudes and over the continental ice sheets (*S3*). The LGM control run also simulates a shoaling of North Atlantic Deep Water and farther northward penetration of Antarctic Bottom Water (*S4*). A 1,800-year LGM equilibrium simulation was branched off from an earlier LGM simulation in order to incorporate the dynamic global vegetation model and to reduce the

SOM, BA_Science, Liu et al., revision2, 05/07/2009

model drift in the deep ocean. The transient simulation was then started at the end of the 1,800-year LGM/DGVM equilibrium run with the transient orbital parameter starting at 22 ka. The transient concentrations of the greenhouse gases (CO_2 , CH_4 and N_2O) were adopted from ref S5. The continental ice sheets were modified approximately once per thousand year according to the ICE-5G reconstruction (S6). The coastlines at LGM were also taken from the ICE-5G reconstruction and were not modified during the simulations in this study.

2: Meltwater Scheme: Since the meltwater flux (MWF) from the retreat of the ice sheets is not well constrained during the last deglaciation, we adopted simple schemes of MWF (Fig.1c) and considered only two regions to impose MWF: one in the North Atlantic region between 50°N and 70°N , and the other in the Gulf of Mexico. From 19 ka to 18.4 ka, the first pulse of MWF was imposed at the rate of 3 m/kyr (1m/kyr = 0.0115 Sv; 1 m/kyr refers to 1 meter of equivalent global sea level rise per thousand year) over the North Atlantic. From 18.4 ka to 17.5 ka, the MWF was linearly increased from 0 to 5 m/kyr in the Gulf of Mexico and from 3 to 5 m/kyr in the North Atlantic. From 17.5 ka to 17.0 ka, the MWF remained at 5 m/kyr in the Gulf of Mexico and linearly increased from 5 to 15 m/kyr in the North Atlantic. Starting from 17 ka, two schemes of MWF were employed to test the sensitivity of the climate system to the rate of the MWF termination. In scheme DGL-B (Fig.1c, blue), the MWF linearly decreased from 20 to 0 m/kyr from 17 ka to 14.2 ka. In scheme DGL-A (Fig.1c, red), the MWF in the Gulf of Mexico was shut off immediately after 17.0 ka, while the MWF in the North Atlantic remained at 15 m/kyr until 14.67 ka when it was abruptly shut off.

Supporting online text

1: Global Temperature Response during Deglaciation: The MWF in the North Atlantic forces significant remote climate responses throughout the globe via climatic teleconnections (S7). Overall, Northern Hemisphere surface temperature evolves similarly to Greenland (Figs.1g-i), but Southern Hemisphere temperature increases monotonically as over the Antarctic. The overall global surface temperature evolution can be seen clearly in the two leading EOFs during the deglaciation (Fig.S3), which are in excellent agreement with the corresponding EOFs derived from surface temperature proxy records from the last deglaciation (S8). The first EOF mode exhibits an overall global warming that tends to increase monotonically as in the Antarctica (Fig.S3a); this mode is caused predominantly by the rising CO₂ and orbital forcing (Fig.1a). In contrast, the second EOF mode exhibits a bipolar seesaw response that evolves similarly to the Greenland temperature (Fig.S3b); this mode is associated with the North Atlantic MWF (Fig.1c) through climate teleconnections.

2. GHG vs Orbital Forcing on BA Warming: To assess the contributions of CO₂ and orbital forcing to BA warming, we performed two sensitivity experiments from H1 to BA that are forced the same as Exp. DGL-A (but with the AMOC effect excluded) except with the transient GHG forcing (CO₂ experiment) and orbital forcing (orbital experiment) imposed separately, keeping all remaining factors at the H1 (17 ka) value. Fig.S4 shows the temperature evolution over Greenland and Antarctic for Exp. DGL-A (black), CO₂ experiment (green solid) and orbital experiment (green dash) from H1 to BA. It is seen

SOM, BA_Science, Liu et al., revision2, 05/07/2009

that the warming in DGL-A is largely contributed by the CO₂ experiment. A further calculation shows that the zonal mean surface warming at high latitudes (>60°) is 3 times greater in the CO₂ experiment than in the orbital experiment (~3°C vs ~1°C). The CO₂ forcing is even more dominant in the tropics (<30° latitude), with a surface warming of ~1°C in the CO₂ experiment, but almost zero or slight cooling in the orbital experiment, the slight cooling in the latter being induced by the reduction of annual insolation associated with the increase of obliquity. For the global average, the surface warming is 6 times larger in the CO₂ experiment than in the orbital experiment (1.51°C vs 0.25°C). From these experiments, we conclude that the warming in Exp. DGL-A from H1 to pre-BA is dominated by the CO₂ forcing.

3. AMOC Hysteresis in CCSM3: The lack of a significant hysteresis in CCSM3 is seen more clearly in the “hysteresis diagram,” in which the model AMOC transport is plotted against the MWF (Fig.S5). As the MWF increases, the AMOC diminishes almost linearly, in contrast to many theoretical and intermediate climate models (*S9-S11*). In addition, as the MWF decreases, the model AMOC largely follows a trajectory of gradual recovery, instead of staying in the off-mode. Furthermore, we have performed dozens of hosing sensitivity experiments similar to those in other models, with the MWF over various regions and of various lengths, in both glacial state and Holocene state (not shown). Our experiments, and similar hosing experiments that have been carried out previously in CCSM3 (e.g. *S12*), all show a recovery of the AMOC as soon as the MWF stops. We have found no evidence of a significant hysteresis and multiple equilibria in CCSM3.

4: Mechanisms for the AMOC Overshoot: At the end of a freshwater pulse, the model AMOC tends to exhibit an overshoot beyond its pre-hosing level, inducing strong warming in the high latitude North Atlantic that lasts a few centuries after the freshwater termination. For the BA warming, this overshoot is associated partly with the strong subsurface warming in response to the long MWF during H1 (Fig.2f), which when the MWF is terminated, destabilizes the convection in the Nordic Sea (*S13*) and heats the atmosphere through an increased upward surface heat flux. The strong CO₂ warming is also important for the melting of sea ice in the Nordic Sea, and in turn the sudden onset of deep convection in this region.

Another possible mechanism for the overshoot is a basin-wide salinity adjustment. This can be demonstrated in a 3-box model that consists of a single polar box that combines the surface and deep polar boxes together for representing the region of deep convection (*S14*) (Fig.S7a) (or a 4-box model with the surface and deep polar boxes separated (*S15*)). In its simplest form, the temperatures are fixed in each box while the salinity is forced by a freshwater flux forcing. This type of box model fundamentally differs from the classical Stommel box model (*S16*) in the inclusion of a deep polar water box that is separated from a deep tropical water box. Damped oscillatory eigenmodes are generated, which lead to a slow overshoot of the AMOC in response to a meltwater pulse as shown in the example in Fig.S7a. In response to a MWF between years 1-300, salinity and the attendant density decrease rapidly in the polar box, reducing the southward pressure gradient at depth and, therefore, the AMOC transport. With the termination of the meltwater flux at year 300, the salinity increases rapidly in the polar box because of

SOM, BA_Science, Liu et al., revision2, 05/07/2009

the fast recovery in the deep convection region. The recovery of the deep tropical salinity, however, lags behind the polar box. As a result, the polar box becomes saltier than the deep tropical box at year 360, generating an equatorward pressure gradient anomaly (relative to pre-hosing) in the deep ocean, which eventually leads to an overshoot of the AMOC beyond its pre-hosing level at year 430, with the peak at year 530. In the meantime, the surface tropical box becomes fresher because of the increased freshwater transport from below. This also contributes to an anomalous equatorward pressure gradient at depth, enhancing the overshoot. The key factor for this overshoot is the slower response time of the deep tropical ocean than the polar region, which creates a delay of the deep tropical salinity, and in turn an anomalous deep pressure gradient that is needed for the AMOC overshoot.

This slow tropical deep ocean recovery for the overshoot appears to be operating in CCSM3 at glacial times, as illustrated in an idealized hosing experiment. For CCSM3, the three ocean boxes are averaged as: surface tropical box (box 1, 45°S – 20°S, 0 - 500-m), polar box (box 2, 35°N – 80°N, 0 – 2000-m) and deep tropical box (box 3, 45°S – 20°S, 500 – 2000-m). The evolution of the AMOC transport and the salinities of the three boxes are plotted for CCSM3 (Fig.S7b) similarly as for the box model (Fig.S7a). The CCSM3 shares a key feature of the overshoot with the box model: the earlier recovery of the polar ocean salinity than the deep tropical salinity. This AMOC overshoot is accompanied by a modest overshoot warming in the Nordic Sea region (3°C over Greenland), but little signal to the south (not shown). In the transient simulations with complete forcing in DGL-A and B, the overshoot is likely to be contributed by both the convection mechanism and the salinity adjustment mechanism.

It remains unclear if the short (centennial) AMOC overshoot in CCSM3 existed in observation. The proxy for AMOC export (Pa/Th ratio in at Bermuda, Fig.1d, S17) does not exhibit an overshoot signal. This lack of overshoot signal, however, could be due to the poor temporal resolution or the long mixing time scale of the proxy itself. In addition, this lack of overshoot may be due to the location of this proxy. Dynamically, the short overshoot event is likely to be recorded more clearly along the deep western boundary current than in the interior ocean, because the deep western boundary current is affected by the upstream perturbation rapidly through the boundary current advection and boundary waves, while the interior ocean is affected by slow adjustment of interior advection and radiating Rossby waves from the eastern boundary. The proxy for AMOC export is located in the interior ocean on the Bermuda Rise (S17) and therefore may not be able to record the overshoot signal. In contrast, a recent high resolution proxy for deep western boundary current speed from the Eirik Drift shows a clear short overshoot at Bølling warming (S18). This location dependence of the overshoot signal is indeed consistent with our model, which shows no overshoot signal in the bottom water near Bermuda, but shows a clear overshoot signal at the Eirik Drift (not shown). Therefore, more high resolution data along the western boundary are needed to assess the existence of an overshoot signal.

5: Is CCSM3 Consistent with Observations for the Abrupt BA Warming? To our knowledge, CCSM3 is consistent with the observed abrupt BA warming within the observational uncertainty, largely because the precise history of MWF prior to BA remains highly uncertain. Indeed, MWF is the derivative of, and therefore much more

SOM, BA_Science, Liu et al., revision2, 05/07/2009

uncertain than, the sea level history. Furthermore, the global sea level change, which accounts for the accumulated MWF of all the sources, has a significant uncertainty in both the timing and magnitude (*S19-S21*). The CCSM3 scenarios for MWF are consistent with some reconstructions, considering the uncertainties. For example, the meltwater during H1 has been suggested to have occurred, in certain regions, in two pulses, H1A and H1B (*S22*). The later pulse H1A occurred between 16 ka and just before BA and may represent the last meltwater pulse whose termination could cause the abrupt BA. In addition, Clark et al. (*S23*) suggest that H1 MWF was bracketed by two major rerouting events into the Hudson River (R8 and R7). The later event (R7) is ~1000 kyr in duration and terminated just before BA. They argued that the combination of R8, H1, and R7 was responsible for the cold period prior to the Bølling, and the final rerouting that terminated R7 was a trigger for the BA warming. Alternatively, the abrupt BA may be caused by a slow stochastic meltwater forcing, via the so called stable collapse in a mono-stable system, as occurred in some climate-ecosystem models (*S24*).

Finally, MWP-1A (*S25, S26*) can also be accommodated in CCSM3. Weaver et al. (*S27*) proposed that the BA was triggered by MWP-1A as a MWF from the Antarctic Ice Sheet, switching the AMOC equilibrium from the off-mode to the on-mode. In CCSM3, however, an Antarctic MWF the same as in ref. *S27* fails to generate a BA warming (not shown). Instead, the MWF weakens the AMOC slightly through the upper ocean transport of freshwater into the North Atlantic, as in other GCMs (*S28*). Nevertheless, MWP-1A can be accommodated as a meltwater discharge from the Antarctic Ice Sheet (*S29*) contemporaneous with (*S30, S31*), instead of preceding (*S18*), the BA, which is possible within dating uncertainties. As such, a large amount of

SOM, BA_Science, Liu et al., revision2, 05/07/2009

meltwater of MWP-1A is “hidden” in the Southern Ocean without a significant global impact. The other possibility is that a significant outflow of MWP-1A entered the Gulf of Mexico as hyperpycnal flow (S32). However, in current model simulations the hyperpycnal flow still is transported eventually into the North Atlantic, where it weakens the AMOC (S33), and recent analyses of runoff records suggests that <13% of the total MWP-1A volume entered the Gulf of Mexico as either a hyperpycnal or hypopycnal flow (S34).

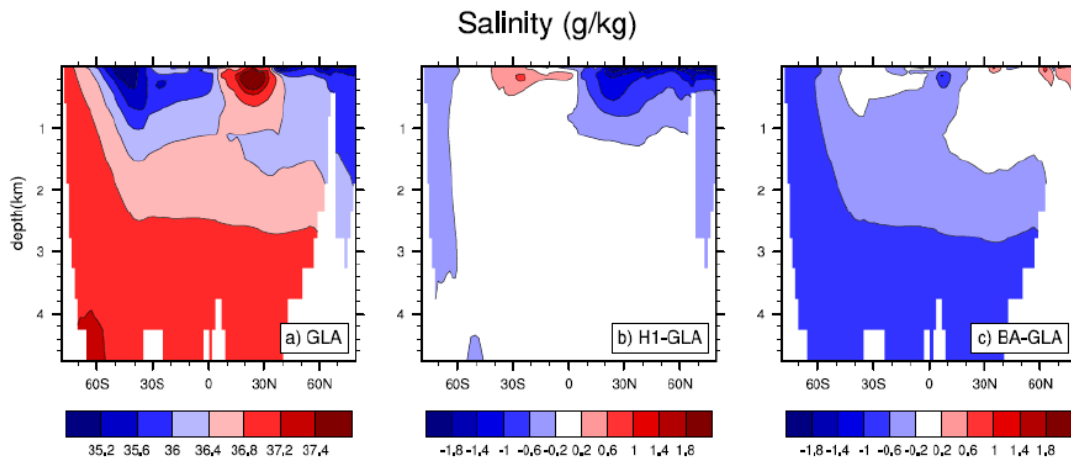


Fig.S1: Atlantic basin zonal mean salinity in exp. DGL-B. for (a) GLA state, (b) H1-GLA, (c) BA-GLA.. It shows the transport of freshwater anomaly from the surface North Atlantic in (b) to the deep ocean through the Antarctic Bottom Water in (c). The continuous evolution of the zonal mean salinity can be seen in the supporting movie 1.

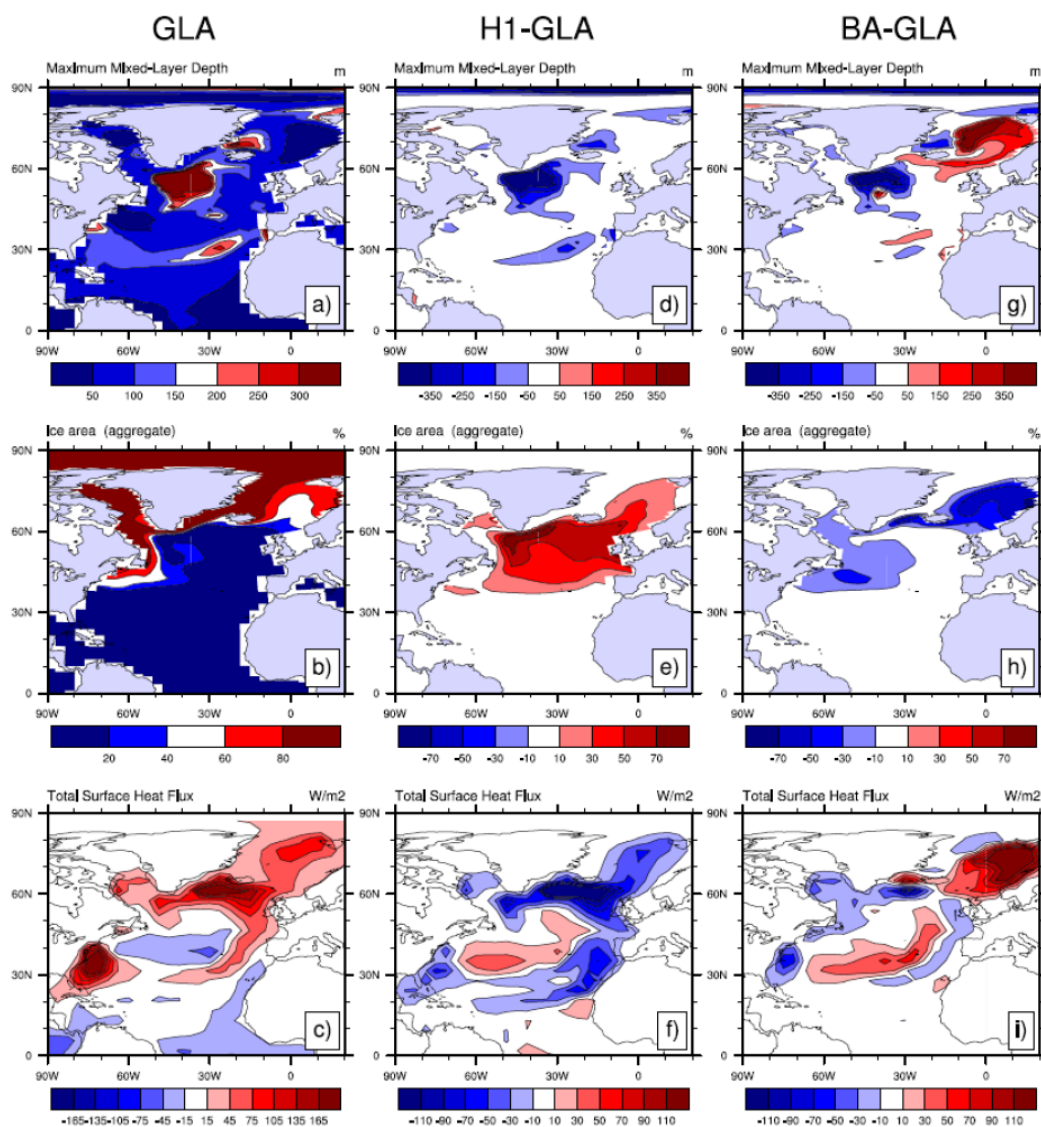


Fig.S2: Model North Atlantic maximum mixed layer depth, (m), sea ice area coverage (%), and surface heat flux (w/m^2 , positive upward) for (a-c) LGM, (d-f) H1-LGM and (g-i) BA-LGM. It is shown that deep convection in Labrador Sea at GLA is shut off at H1, with a sea ice expansion and loss of heat flux to the atmosphere. Deep convection is then resumed in the East Greenland Sea at BA, with the retreat of sea ice and a significant release of heat flux into the atmosphere, similar to a Holocene simulation (not shown).

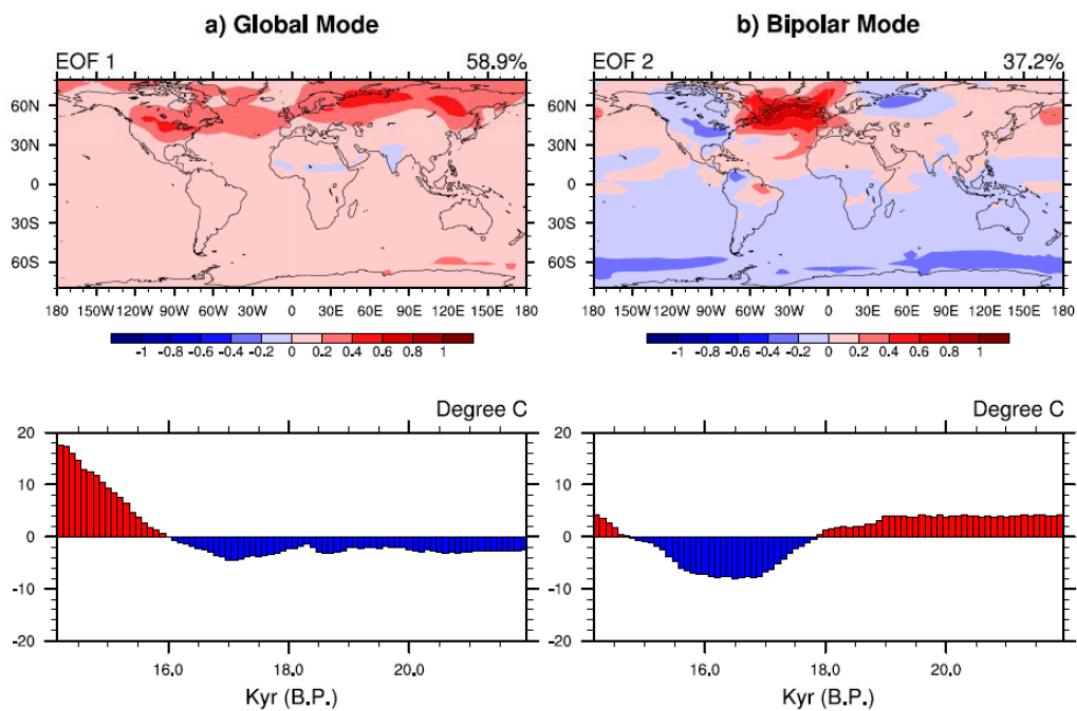


Fig.S3) (a) EOF1 and (b) EOF2 (upper pattern, lower time series) of global surface air temperature in Exp. DGL-B. The EOF1 exhibits a global warming with the evolution similar to Antarctic temperature, while EOF2 exhibits a bipolar seesaw with the evolution similar to Greenland temperature. These two EOFs are in good agreement with the EOFs of the SST reconstruction of ref. S8.. (EOF is normalized, while the time series has the unit of °C).

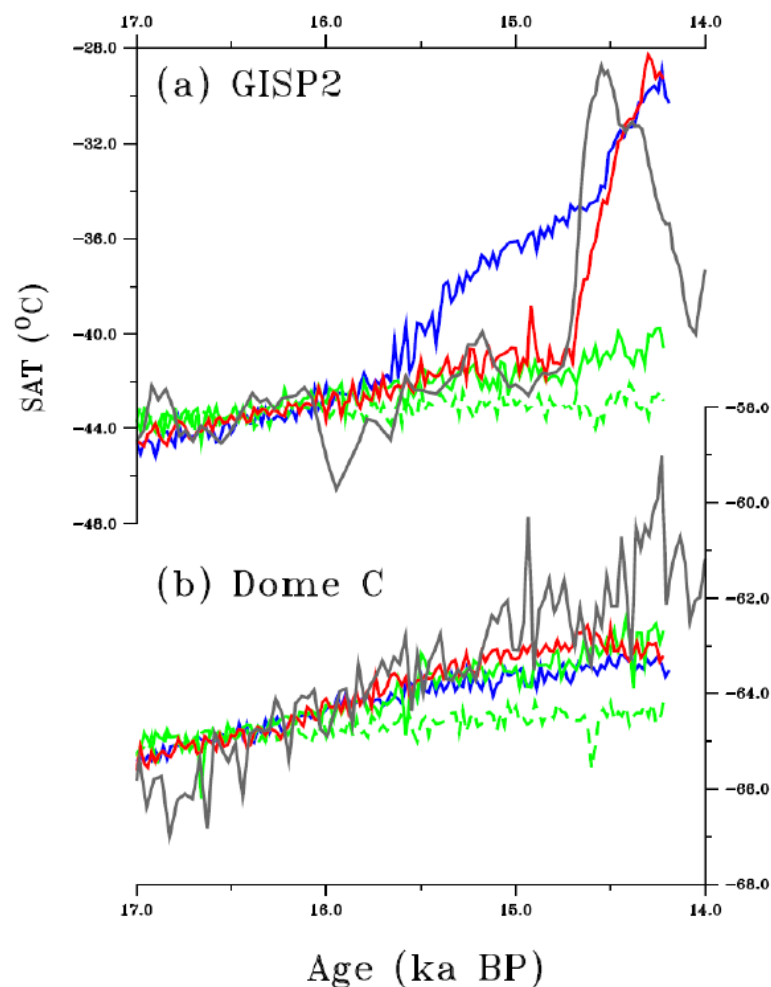


Fig.S4: Temperature (20-year running mean) evolution at (a) Greenland and (b) Dome C from H1 to BA for two sensitivity experiments that are forced the same as in Exp. DGL-A except that the transient CO₂ (CO₂ experiment, solid green) and insolation (orbital experiment, dash green) forcing is imposed separately starting at 17 ka. For comparison, the corresponding temperature evolution in the observation (black), Exp. DGL-A (red), DGL-B (blue) are also plotted the same as in Fig.1. It is clear that the warming in DGL-A is caused predominantly by the increase of CO₂.

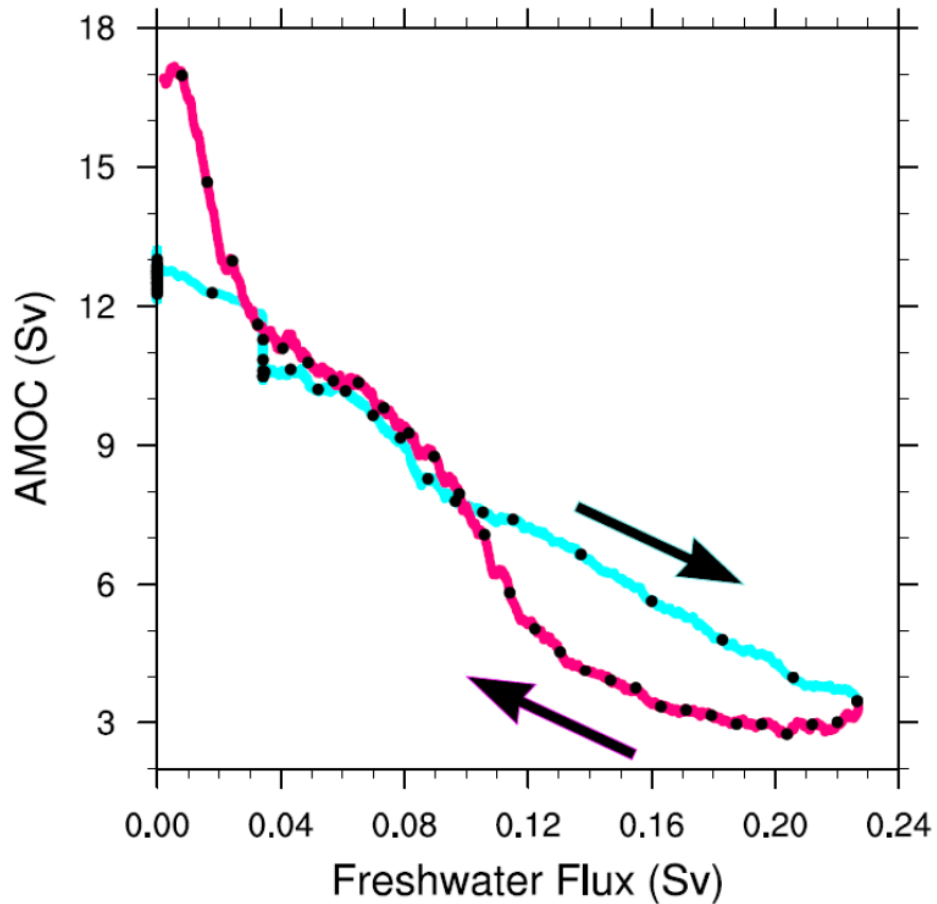


Fig.S5: "Hysteresis diagram" showing the AMOC transport (maximum transport below 500-m) (after a 50-year running mean) as a function of the prescribed meltwater flux in Exp. DGL-B. (Each dot for a 100-yr mean. Blue for the early part and purple for the later part). The AMOC shows no significant hysteresis: when the freshwater flux is increased, the AMOC diminishes almost linearly; when the freshwater flux is reduced, the AMOC transport can barely stay at the constant level of a AMOC-off state.

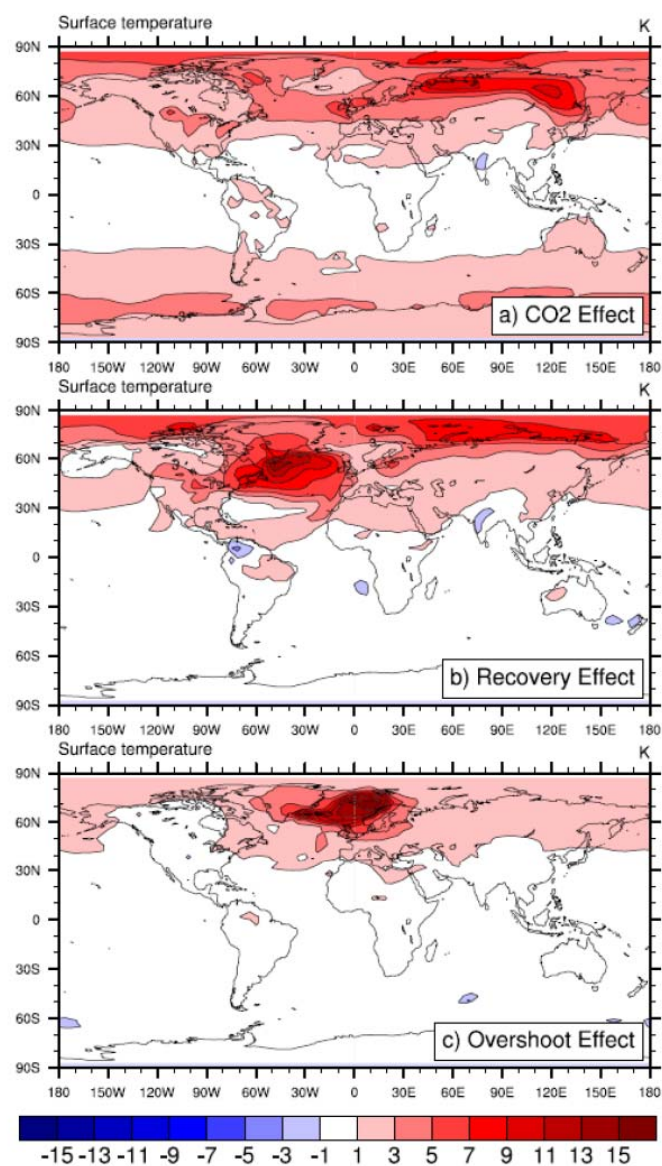


Fig.S6: Three components of the total BA warming above H1 in surface air temperature ($^{\circ}\text{C}$) (BA-H1 in Fig.3b) as estimated in Exp. DGL-A. (a) Radiative effect due to CO_2 (PreBA-H1), (b) Recovery Effect (REC- PreBA), (c) Overshoot effect (BA-REC). (each state is defined in Fig.1d). The CO_2 effect is predominantly hemispherically symmetric, while the other two are confined in the North Atlantic.

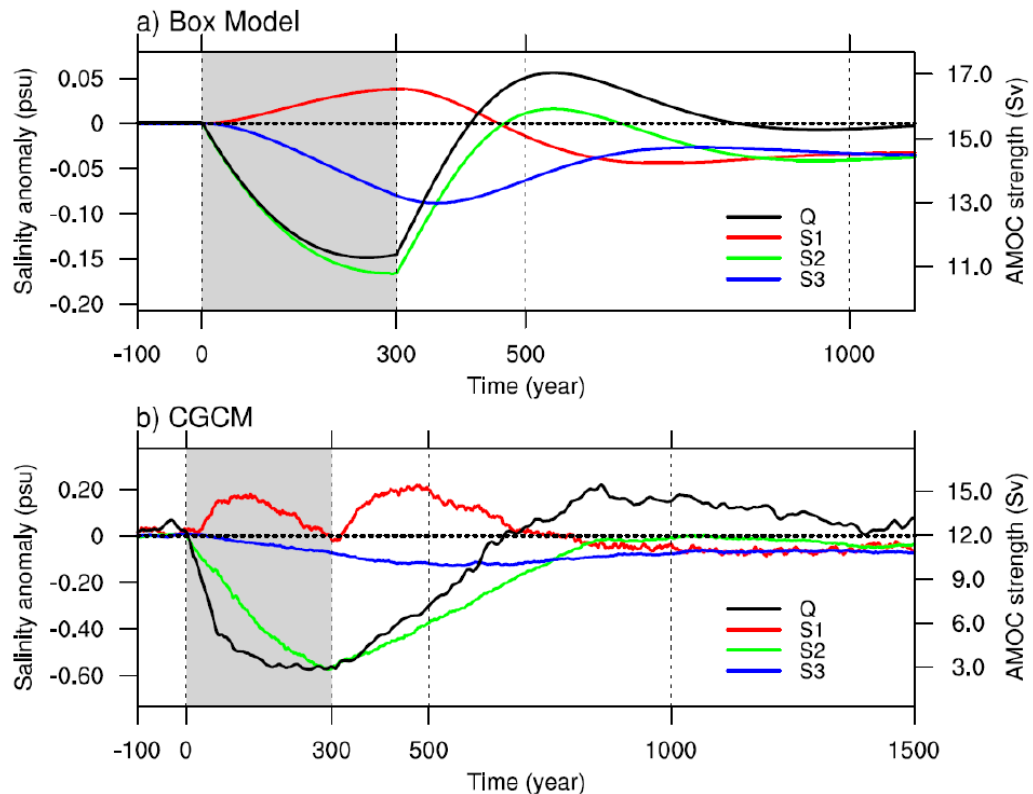


Fig.S7: Time series for AMOC transport (black) and box salinities, for an idealized hosing experiment in (a) a 3-box model and (b) the CCSM3 (salinity in ppt and transport in Sv.), illustrating a mechanism of AMOC overshoot associated with salinity adjustment. (see SOM, text 4 for more details). The box model is a hemispheric 3-box model, with a surface tropical box (box 1, red), a polar box from the surface to the bottom (box 2, green) and a deep tropical box (box 3, blue) (S9). The boxes are of equal latitudinal width for the tropical and polar boxes, and equal thickness for the surface and deep tropical boxes. A perturbation freshwater pulse is added into the polar box at a constant rate from $t=1$ to 300 years. The AMOC transport anomaly (black) decreases during hosing, and recovers subsequently, with an overshoot peak at $t=520$ years. In the recovery stage, the negative salinity anomaly recovers faster in the polar box (green) than in the deep tropical box (blue), generating an anomalous southward deep pressure gradient and therefore an overshoot of the AMOC. (b) Similar to the box model, but for an idealized hosing experiment in CCSM3 with the meltwater flux imposed over the North Atlantic at the constant rate of 33-mslv/1000-yr for 300 years on the glacial state (from 19 -18.7ka), The Atlantic basin is partitioned into box 1 (45°S – 20°S, 0-500-m), box 2 (35°N – 80°N, 0 – 2000-m) and box 3 (45°S – 20°S, 500 – 2000-m). Qualitatively, the evolution in CCSM3 seems to resemble that of the box model.

References for SOM

- S1: W. D. Collins et al. *J. Climate*, **19**, 2122 (2006)
- S2: S. G. Yeager, C. A. Shields, W. Large, J. Hack, *J. Climate*, **19**, 2545 (2003)
- S3: B. L. Otto-Bliesner et al., *J. Clim.*, **19**, 2526 (2006)
- S4: B. L. Otto-Bliesner et al., *Geophys. Res. Lett.*, **34**, L12707, doi:10.1029/2007GL029475 (2007).
- S5: F. Joos, R. Spahni, *Proc Natl Acad Sci*, **105**, 1425, doi:10.1073/pnas.0707386105 (2008).
- S6: W. R. Peltier, *Annu. Rev. Earth Planet. Sci.*, **32**, 111 (2004)
- S7: Z. Liu, M. Alexander, *Rev. Geophys.*, **45**, RG2005, doi:10.1029/2005RG000172 (2007).
- S8: P. U. Clark, N.G. Pisias, T.F. Stocker, A.J. Weaver, *Nature*, **415**, 863 (2002)
- S9: H. Dijkstra, *Tellus*, **59A**, 695-705 (2007)
- S10: S. Rahmstorf, *Nature*, **378**, 145 (1995).
- S11: S. Rahmstorf, et al., *Geophys. Res. Lett.*, L23605, doi:10.1029/2005GL023655 (2005)).
- S12: A. Hu, B. L. Otto-Bliesner, G. A. Meehl and W. Han, *J. Climate*, **21**, 2239-2258 (2008)
- S13: J. Mignot, A. Ganopolski, A. Levermann, *J. Clim.*, **20**, 4884 (2007)
- S14: E. Tzipermann, P. Ioannou, *J. Phys. Oceanogr.*, **32**, 3427 (2002)
- S15: E. Tzipermann, J. Toggweiler, Y. Feilks, K. Bryan, *J. Phys. Oceanogr.*, **24**, 217 (1994)

SOM, BA_Science, Liu et al., revision2, 05/07/2009

S16: H. Stommel, *Tellus*, **13**, 224 (1961)

S17: J. F. McManus, R. Francois, J-M., Gherardi L. Keigwin , S. Brown-Leger, *Nature*,
428, 834 (2004)

S18: J. Stanford et al., *Paleoceanography*, **21**, PA4103, doi:10.1029/2006PA001340
(2006)

S19: Y. Yokoyama, K. Lambeck, P. Deckker, P. Johnston, L. Keith Fifield, *Nature*,
406,713 (2000)

S20: P. U. Clark, A.C. Mix, *Quat. Sci. Rev.*, **21**, 1 (2002)

S21: W. Peltier, R. Fairbanks, *Quat. Sci. Rev.*, **25**, 3322 (2006)

S22: E. Bard, F. Rostek, J-L Turon, S. Gandrau, *Science*, **289**, 1321 (2000)

S23: P. U. Clark et al., *Science*, **293**, 283 (2001)

S24: Z. Liu, Y. Wang, R. Gallimore, M. Notaro, I. C. Prentice, *Geophys. Res. Lett.*, **33**,
L22709, doi:10.1029/2006GL028062 (2006).

S25: R. Fairbanks, *Nature*, **342**, 637 (1989)

S26: T. Henebuth, K. Stattegger, P. Grootes, *Science*, **298**, 1033 (2000)

S27: A. J. Weaver,, O. A. Saenko, P. U. Clark, J. X. Mitrovica, *Science*, **299**, 1709 (2002)

S28: R. Stouffer, D. Dsidov, B. Haupt, *J. Climate*, **20**, 436 (2007)

S29: P. U. Clark et al., *Paleoceanography*, **11**, 563 (1996)

S30: T. Hanebuth, K. Stattegger, P.M. Grootes, *Science*, **288**, 1033 (2000)

S31: K.B. Cutler et al., *Earth Planet. Sci. Lett.*, **206**, 253 (2003)

S32: W. Peltier, G. Vettoretti, M. Stastna, *Geophys. Res. Lett.*, **33**
doi:10.1029/2005GL025251 (2006)

SOM, BA_Science, Liu et al., revision2, 05/07/2009

S33: D. Roche, H. Renssen, S. Weber, H. Goosse, *Geophys. Res. Lett.*, **34**,
doi:10.1029/2007GL032064 (2007)

S34: A.E. Carlson, *Quat. Sci. Rev.*, **28**, in press (2009)